AGU100 ADVANCING EARTH AND SPACE SCIENCE

Geophysical Research Letters

RESEARCH LETTER
10.1029/2018GL078977

Key Points:
- The lag in timing of extratropical cyclone dynamical strength compared to precipitation is explained by changes in environmental moisture
- The life cycle of precipitation is governed by both cyclone dynamical age and cyclone latitude

Correspondence to:
J. F. Booth,
jbooth@ccny.cuny.edu

Citation:
Booth, J. F., Naud, C. M., & Jeyaratnam, J. (2018). Extratropical cyclone precipitation life cycles: A satellite-based analysis. *Geophysical Research Letters*, *45*, 8647–8654. https://doi.org/10.1029/2018GL078977

Received 29 MAY 2018
Accepted 10 AUG 2018
Accepted article online 20 AUG 2018
Published online 27 AUG 2018

Extratropical Cyclone Precipitation Life Cycles: A Satellite-Based Analysis

James F. Booth[1,2,3], Catherine M. Naud[2,4], and Jeyavinoth Jeyaratnam[1,3]

[1]Earth and Atmospheric Sciences, City University of New York–City College, New York, NY, USA, [2]NASA GISS, New York, NY, USA, [3]Earth and Environmental Sciences Department, The Graduate Center, City University of New York, New York, NY, USA, [4]Applied Physics and Applied Mathematics, Columbia University, New York, NY, USA

Abstract Although extratropical cyclones are the most common midlatitude storms, the relationship between their precipitation life cycle and dynamical strength life cycle has not been thoroughly analyzed. Given that thermodynamic heat exchanges associated with precipitation impact cyclone circulation, there is a need to understand the precipitation/dynamics relationship. Based on Integrated Multi-satellitE Retrievals for Global Precipitation MeasurementGPM precipitation and Lagrangian cyclone tracks, the precipitation maximum occurs prior to the dynamical strength maximum 70% of the time. The lag in timing is consistent with the difference in cyclone precipitable water vapor at the two peaks. Conditional subsetting of the cyclone composites shows that if the precipitable water vapor distribution is constrained to be equal throughout the composite life cycle, the precipitation peak occurs very near the time of the peak in cyclone dynamical strength. Thus, the boost in dynamical strength caused by latent heat associated with precipitation manifest itself with little to no time lag.

Plain Language Summary Extratropical cyclones are the most common storms in the midlatitudes. These storms generate strong precipitation and winds. The heating within the troposphere that occurs during the formation of the cyclone''s precipitation can increase the cyclone''s circulation strength, which relates closely to the winds. This study analyzes the timing of the evolution of precipitation and cyclone strength using satellite observations of precipitation. The results show that the peak in precipitation usually occurs prior to the peak in circulation, and the cause is related to moisture availability. A separate analysis in which cyclones are selected in a manner that fixes the moisture availability at each time step throughout the life cycle indicates no lag between precipitation and circulation peaks. Thus, it seems likely that any boost in dynamical strength that is caused by the precipitation occurs with little to no lag in time.

1. Introduction

Extratropical cyclones (ETCs) are the primary weather makers of the midlatitudes. Their impacts can depend on their dynamical strength and their precipitation. These two properties are linked: The condensation within an ETC generates precipitation and also provides energy that increases the dynamical strength of the ETC (e.g., Ahmadi-Givi et al., 2004; Emanuel et al., 1987; Stoelinga, 1996). Understanding all aspects of this coupling between precipitation and cyclone dynamical strength is increasingly important because anthropogenic climate change will increase midlatitude moisture (Held & Soden, 2006). With this as motivation, our analysis focuses on the observed relationship between the time evolution of ETC precipitation and dynamical strength.

The life cycle of an ETC is often characterized based on cyclone dynamical strength. A cyclone typically exhibits an intensification phase, a peak, and a decaying phase, which can be identified using the sea level pressure (SLP) at the center, the vorticity, or surface wind speed. Using such a definition, previous work has shown that the peak in precipitation occurs 18- to 12-hr prior to the peak in dynamical strength (Bengtsson et al., 2009), or perhaps even earlier (Michaelis et al., 2017; Rudeva & Gulev, 2011). This delay in the dynamical peak could be related to the fact that latent heat release plays a role in cyclone intensification and that, perhaps, the response of the dynamical strength to latent heating takes time. However, using a larger data set of cyclones, Hawcroft et al. (2017) found little to no difference in the timing of peak precipitation and dynamical strength in reanalysis data. Given that other studies have documented the dependence of ETC precipitation on both strength and precipitable water vapor (PWV; Field & Wood, 2007; Pfahl & Sprenger, 2016), an alternate hypothesis to explain the timing lag is that cyclone PWV decreased in the Bengtsson et al. (2009) and Rudeva and Gulev (2011) studies. Indeed, Rudeva and

Gulev (2011) indicate that their study focused on specific types of cyclones in which it happened to be the case that the PWV within the cyclone decreased as the cyclones grew in dynamical strength. Thus, the peak in precipitation leading the peak in dynamical strength may be a consequence of PWV differences. Herein, we provide an explanation for these previous results showing a lag in peak intensity and benchmark the life cycle of precipitation based on satellite observations.

Recent advances in merged satellite precipitation products make it possible to characterize the behavior of precipitation over the course of an ETC life cycle. The Global Precipitation Measurement (GPM; Skofronick-Jackson et al., 2017) core observatory provides microwave and radar retrievals of precipitation extending from the tropics into the midlatitudes. The analysis presented here utilizes the Integrated Multi-satellitE Retrievals for GPM (IMERG; Huffman et al., 2017) product. The approach taken here is unique from previous studies, because we utilize a compositing approach that generates subsets of cyclones that have similar distributions of cyclone-local PWV for each dynamical life cycle stage. This analysis identifies and explains the most likely cause of the relationship between the time evolution of precipitation in ETCs as compared to the evolution of the dynamical strength.

2. Data and Methods

IMERG version 5 (Huffman, 2017) is a global, gridded, merged precipitation data set, of 0.1°and 30-min spatial and temporal resolution. To match the resolution of the reanalysis data used to identify the ETCs, we use IMERG data averaged over 6 hr, centered on the time step of interest. The product merges a vast number of satellite microwave precipitation estimates, with microwave-calibrated infrared satellite estimates and precipitation gauge analysis for the GPM era. An assessment of IMERG for ETCs shows that it has differences with single-platform data sets (e.g., the GPM radar-radiometer combined product; Grecu et al., 2016), some of which are systematically related to column water vapor (Naud et al., 2018). However, the analysis herein is designed in a manner that minimizes the issue. The time period used for this analysis is 2014–2017. We only consider the cold seasons, that is, March–October for the Southern Hemisphere and November–April for the Northern Hemisphere. Because we found similar results for the two hemispheres, we combine the data from both in a single analysis.

The primary methodology of this study is cyclone-centered analysis, which entails identifying ETCs and studying the conditions in a frame relative to each cyclone's center. First, ETC tracks are identified by applying the Lagrangian cyclone tracker of Bauer et al. (2016) to 6-hourly SLP fields from the ERA-Interim reanalysis (Dee et al., 2011). The tracker identifies individual cyclone centers as local minima in SLP and then links the centers in time to make tracks. Detection of a cyclone is based on the strength of the SLP anomaly and whether or not it moves geographically as time evolves. Thus, the first detection and final detection of a cyclone track can be associated with the cyclone's genesis and lysis, respectively. Throughout the paper, cyclones will refer to individual 6-hourly snapshots and tracks will refer to the entire life cycle of the ETC. This analysis uses cyclones over land and ocean but is limited to the cyclones whose centers are found between 25° and 65° for both hemispheres.

For each cyclone, using a fixed-distance radius (500 km unless stated otherwise) we identify the cyclone-centered IMERG precipitation, 850-hPa relative vorticity (hereafter, vorticity), and PWV from ERA-Interim. We multiply Southern Hemisphere vorticity by -1 when we combine data from the two hemispheres. Cyclone-centered averages of vorticity are used in sorting the data. Sensitivity tests using an averaging radius of 250 km and 750-km radii to average the vorticity are discussed in section 3. For area-averaged precipitation, we ignore points with zero precipitation. Thus, we are calculating the rain rate when raining. This is done to allow the distributions of area-averaged precipitation to have a fatter tail, and it does not impact the results qualitatively. Hereafter, precipitation will refer to the value calculated when ignoring zero precipitation rates in the average.

The ETC life cycles are based on the time evolution of the vorticity. To do this, we calculate cyclone-averaged values, which are averages for the area within a fixed radius around the cyclone center. For each track, the maximum cyclone-average vorticity corresponds to $t = 0$. All time points along the track prior to peak are negative, and times after the peak are positive. Vorticity is used for dynamical strength of ETCs in place of SLP or surface winds (1) because it has less dependence on the background state than SLP (e.g., Hoskins &

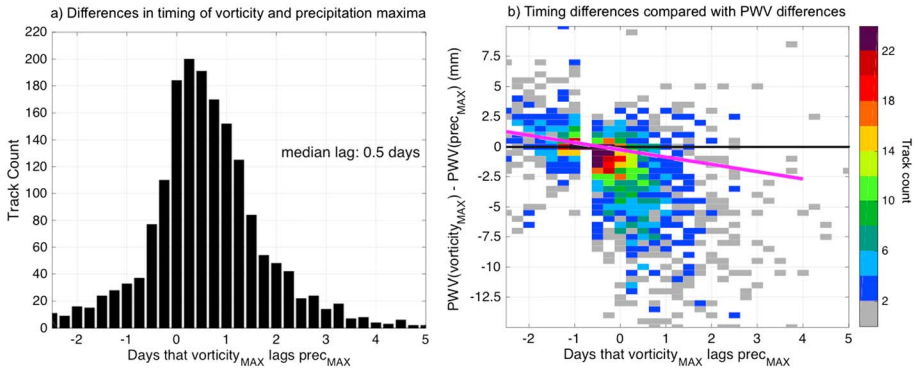

Figure 1. Comparison of dynamic and precipitation life cycles per track: (a) The difference in track-relative timing of the maximum in dynamical strength (vorticityMAX) and the precipitationMAX per cyclone track. (b) Comparison of the difference in timing and the difference in cyclone-averaged precipitable water vapor (PWV). Color shows the track count per bin. The magenta line shows the fit, which has a slope of −0.61 days of lag per PWV difference in millimeters. Total tracks in the analysis: 1,764. The Pearson correlation coefficient in (b), −0.57, is statistically significant at the 99th percentile based on a *t* test.

Hodges, 2002) and (2) because surface friction, which differs significantly over land compared to ocean, has a larger impact on surface winds than 850-hPa vorticity.

After assigning life cycle ages to each cyclone, we group them based on their age. Thus, for example, all cyclones in the $t = -6$ set for vorticity occur 6 hr prior to the vorticity maximum for that cyclone's tracks. We refer to these as life cycle sets. Because we consider tracks of different durations, the life cycle sets do not all contain cyclones from the exact same tracks. This inconsistency is also caused if tracks with the same duration have the maxima in vorticity or precipitation occurring at different points along the track. To address this issue without severely limiting the size of our data set, we remove all tracks in which the maxima for vorticity and precipitation occur less than 12 hr after the first time step of the track or less than 12 hr before the final time step of the track. After applying this filter, the total number of tracks in the analysis is 1,764. The total number of individual cyclones in the analysis is 31,764. The small number of tracks compared to cyclones reflects our choice of terminology: Cyclones are the 6-hourly snapshots along a track. Each track's duration is at least 30 hr (which means it includes six individual cyclone instances). The median duration for the tracks is 4.25 days.

The constraint that requires the precipitation and vorticity maxima to occur two time steps away from the track end points does not impact the results. However, it does increase the likelihood that the life cycle sets contain cyclones from the same track for the 24-h period centered on the vorticity maximum and the 24-hr period centered on the precipitation maximum. This constraint also means that there are more cyclones in the data set whose life cycle age is ±12 hr from the peak. For ages outside of those ranges, we group the cyclones using adjacent time steps. Finally, before calculating multicyclone averages for any life cycle age we randomly subsample each age subset so they have the same number of cyclones. This allows a clean comparison of the distributions of cyclone properties for each age subset.

3. Results

Using the ETC life cycle information, we compare the relative timing of the vorticity and precipitation maxima per track. We find that the vorticity maximum occurs after the precipitation maximum in 70% of the cyclones, with a median delay of 12 hr (Figure 1a). Ten percent of the time, the peaks are coincident, leaving only 20% of the time that the peak in vorticity occurs before the peak in precipitation. Furthermore, the length of the delay between the precipitation peak and the vorticity peak is linearly related to the magnitude of the difference in mean PWV at the two times (Figure 1b). This suggests that relative differences in the life cycle of ETC precipitation and vorticity may primarily relate to how much moisture is available to the cyclone at a given time. The changes in PWV during a track life cycle are strongly correlated with changes in latitude, with the PWV decreasing and the cyclones moving poleward in the course of their life cycles. Figure 1 suggests

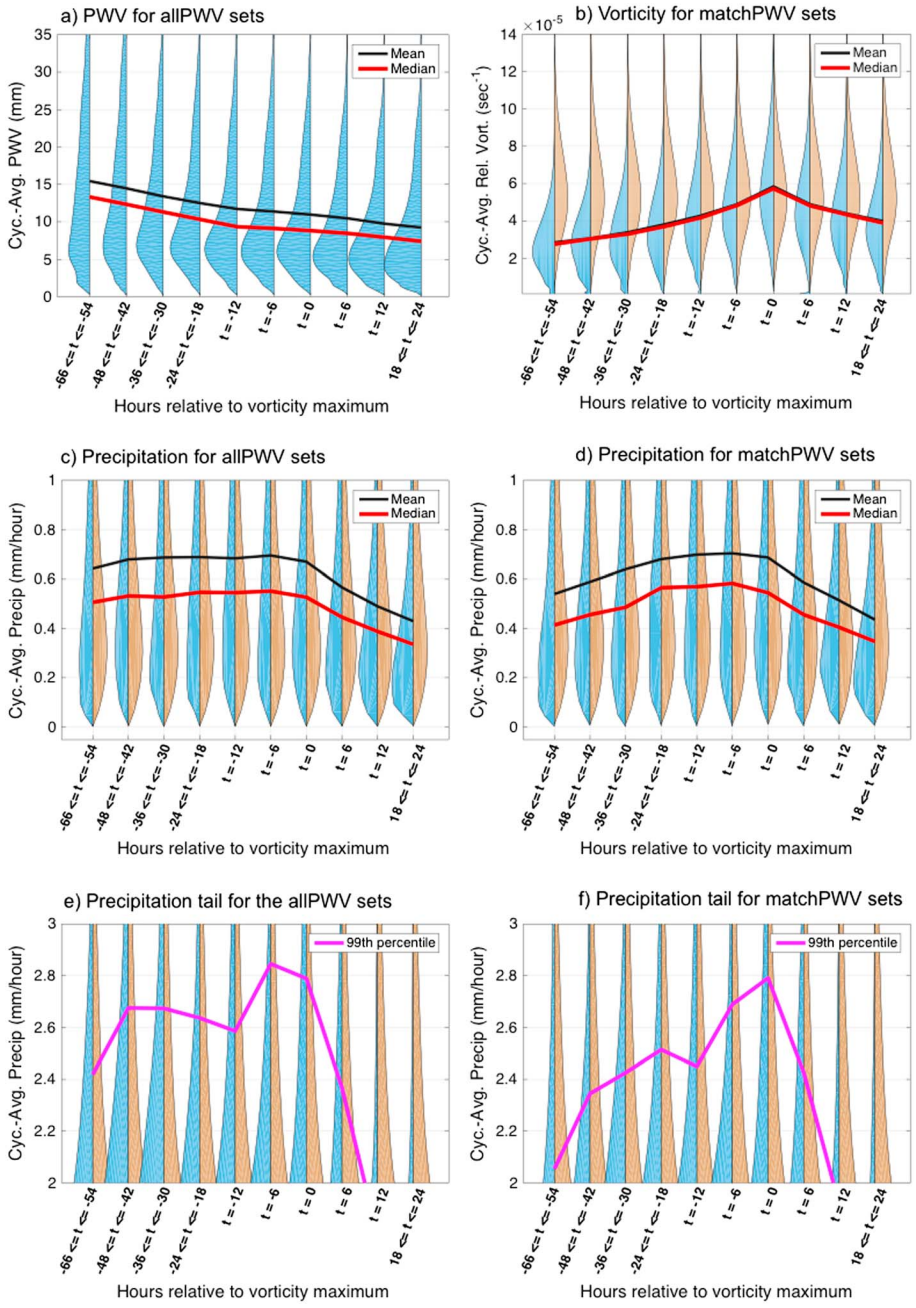

Figure 2. Time evolution of cyclone-averaged variables sorted based on cyclone vorticity. (a) Precipitable water vapor (PWV) for allPWV, (b) vorticity for matchPWV, (c and d) precipitation in the range from 0 to 1 mm/hr, and (e and f) precipitation in the range from 2 to 3 mm/hr. In all panels, blue shows the distribution of the variable at the time indicated on the *x*-axis. When shown, brown shows the distribution for the time of the vorticity maximum (repeated on every time step for comparison). In panels (a–d), black shows the multicyclone mean for each time step and red shows the median. In panels (e and f), pink shows the 99th percentile for each time step. Number of cyclones included in the analysis per life cycle age: 1,338 for allPWV (left) and 1,006 for matchPWV (right).

that the life cycle differences found in Rudeva and Gulev (2011) are due to the fact that ETCs in the North Atlantic propagate northward into regions of lower PWV as they strengthen.

The analysis discussed above compared strength and precipitation characteristics per ETC track. Next we consider the behavior based on the life cycle subsets. First, we consider the distribution of PWV for the cyclones in each life cycle set. Figure 2a shows that as the age increases, the PWV available to the cyclone decreases. It

can be seen not only in the multicyclone mean values but also in the changes in the shape of the distributions of cyclone-averaged PWV for each life cycle set.

Given the strong relationship between PWV and track life cycles, we take advantage of the compositing approach to arrange cyclones in a manner that breaks this relationship. To do this, we create a subset of cyclones, for each life cycle set, that has a distribution of average PWV that match; that is, we generate a target distribution and randomly sample each life cycle set to create a subset that matches the target. To ensure that the random sampling does not introduce a bias, we repeat the subsampling analysis 50 times and then consider the distribution of the accumulated subsets per life cycle (not shown for PWV). This collection of cyclones in which the PWV distributions match for each life cycle subset will be referred to as *matchPWV*, and we will compare between this set and the set of all cyclones, referred to as *allPWV*.

Sorting matchPWV based on vorticity results in a clear time-evolving multicyclone mean vorticity versus cyclone age (Figure 2b). The distributions of vorticity for each life cycle set are also easy to distinguish: Prior and post vorticity maximum, the distributions have a lot more weight in the weak values. This result suggests that the random sampling did not distort the characteristic differences in vorticity that are expected when we sort based on vorticity life cycle.

The evolution of precipitation sorted based on the life cycle of vorticity for the allPWV cyclone set shows that the multicyclone mean is relatively constant from 48 hr prior until the time of the vorticity peak (Figure 2c). After the peak, the multicyclone mean decreases monotonically. Results are shown out to 24 hr, but the decrease continues for the following day as well. The distributions of cyclone-averaged precipitation also show little difference for 48 hr prior until the time of peak vorticity, after which time the distribution shifts to smaller values. If we consider matchPWV, then the multicyclone mean precipitation gradually increases from 66 to 12 hr before the vorticity peak, and then it plateaus (Figure 2d). By comparing the distributions of precipitation at any time with that at time of maximum vorticity, one can see that the differences in the multicyclone means are caused by small differences in the shapes of the distributions. Only the distributions prior to 2 days and 12 hr after peak vorticity are noticeably different from the distribution at peak vorticity. This is a consequence of combining such a diverse range of cyclones. Overall, the analysis shows that based on the average over more than 1,000 cyclones, the precipitation maximum occurs at the same time as the vorticity maximum. However, the multicyclone mean precipitation is equally strong prior to the vorticity maximum, and duration of this plateau is about 18 hr if the data are sorted to constrain the PWV distributions.

Analysis of the strongest precipitation supports this result. The 99th percentile for the life cycle sets of precipitation peaks at 6 hr prior to vorticity maximum in the allPWV and at the same time as the vorticity maximum in the matchPWV case (Figures 2e and 2f). For these strong precipitation data, the impact of sorting PWV is clearer: The allPWV case has stronger precipitation at 18 to 60 hr prior to the vorticity maximum as compared to the matchPWV case. As was the case for the base of the distributions, the tails show minor differences between the different life cycle times. However, comparing the distribution tails at a given time with that at peak vorticity indicates a clear shift in the precipitation amounts: The largest precipitation occurs more often when the cyclones are the strongest dynamically.

The analysis reported in Figure 2 utilized cyclone-averaged relative vorticity with a 500-km radius to define dynamical strength and life cycle. Another common metric used to define cyclone lifecycles is SLP (e.g., Booth et al., 2018; Pfahl & Sprenger, 2016). If we carry out the analysis using SLP to define cyclone dynamical strength, the timing of the peak in precipitation is prior to the SLP minimum. This more distinct lag is most likely related to the latitudinal dependence of mean-state SLP (e.g., Ulbrich et al., 2009). The use of 500 km for area-averaging the relative vorticity is also debatable. We repeated the analysis defining the life cycle using a smaller radius, 250 km, and found very similar results. The duration of the plateau in precipitation decreased from 18 to 12 hr, but, most importantly, the difference between the allPWV and matchPWV sets was identical to the result shown in Figure 2. Using a larger averaging radius (750 km) also did not impact this result.

As the final step in understanding ETC precipitation life cycles, we examine precipitation composites. Cyclone compositing provides a map view of ETC precipitation, clouds, or circulation, (e.g., Chang & Song, 2006; Hawcroft et al., 2012; Naud et al., 2018), and it is a useful tool for comparing general circulation models with observations (e.g., Bauer & Del Genio, 2006; Booth et al., 2013; Catto et al., 2010). Cyclone-centered composites do not reflect the typical spatial pattern of individual ETCs. Instead, they should be viewed as two-

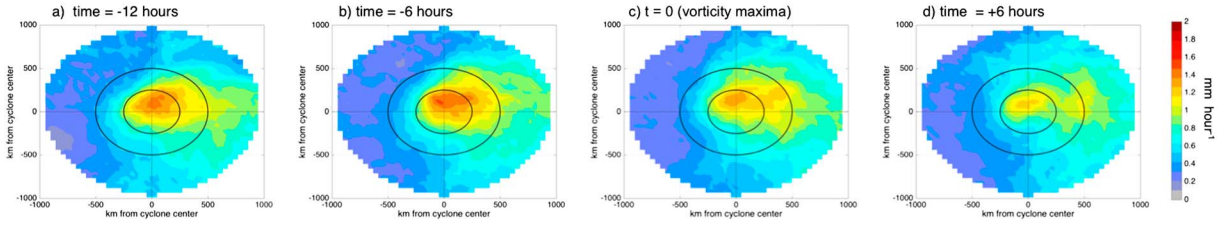

Figure 3. Cyclone-centered composites of precipitation, sorted by cyclone age, for Northern Hemisphere and Southern Hemisphere, 2014–2017. In each panel, the inner black circle indicates a radius of 250 km. The outer black circle is 500 km. There are 1,006 cyclones per composite.

dimensional histograms weighted by the intensity of the variable being composited. Furthermore, the composites here show averages of nonzero precipitation rates, and so the stronger values indicate more weight in the high tail of the distribution. For our composites, we include both hemispheres by reversing the latitudes for Southern Hemisphere cyclones. We only show results for the matchPWV because it is the set that addresses the question of precipitation evolution in the absences of changes in PWV.

In the composite, the maximum multicyclone mean rain rates occur 6 hr prior to the vorticity peak, that is, $t = 0$ (Figure 3b). Furthermore, at 12 and 6 hr prior to the vorticity peak, the precipitation within 250 km of the cyclone center is stronger than the precipitation for the same region at $t = 0$ (Figure 3). On the other hand, for the region 250 to 500 km from the cyclone center there is stronger precipitation at $t = 0$ (Figure 3c). Thus, the plateau as seen in the cyclone-centered averages is due to a trade-off between precipitation close to and farther from the cyclone center. We interpret these results as follows. In an ETC, most of the rainfall occurs along the warm and cold fronts and between the two in the warm sector, near the cyclone center (e.g., Naud et al., 2018). As the ETC grows in dynamical strength, the strongest precipitation along the fronts often migrates away from the central SLP minimum. At the same time, the distance between the fronts decreases, shrinking the spatial size of the region of strong precipitation. Because the distance between the fronts and the cyclone center varies cyclone to cyclone, there is more variability in the location of the strongest precipitation at maximum vorticity ($t = 0$), as compared to earlier in the cyclone life cycle. As a result, the composite at the times of the track vorticity maxima shows moderately strong precipitation values spread out over a larger region.

4. Conclusions

The analysis presented here shows that in individual ETCs, the precipitation peak often occurs prior to the maximum in ETC dynamical strength. This appears to be strongly linked to the change in PWV available to the ETC. The change in PWV is partially due to the poleward movement of the ETC as they grow in dynamical strength, and this is true in both hemispheres. Over the full course of their life cycles, Northern Hemisphere tracks move toward the pole more than those in the Southern Hemisphere; however, there is little to no difference in the changes in PWV (or latitude) between the times of the maximum in precipitation and dynamical strength for the two hemispheres. All of these initial results are based on the analysis of ETCs per track.

Sorting subsets of cyclones by age based on dynamical strength, while also requiring that the PWV (for the subset) does not change with time, allowed us to test if the lag in timing for dynamical strength relative to precipitation is related to changes in cyclone PWV. The analysis shows that the multicyclone precipitation for 12 hr prior until the time of the maximum in dynamical strength is nearly the same. The caveat on this analysis is the fact that the life cycle subsets do not include all cyclones from each track; however, the life cycles of these mix-matched cyclones strongly suggest that PWV is the cause of the lag between precipitation and circulation.

It is known that condensation within an ETC can strengthen the circulation, but timing of the circulation response is not fully understood. If there was a delay, then we might expect some difference in the timing of the peak in precipitation and the peak in dynamical strength. Physical explanations for the link between the condensation and the dynamical strength, based on either potential vorticity or vertical stability within the cyclone (e.g., Wernli & Davies, 1997), suggest that the dynamical response of the ETC should be nearly instantaneous. One might argue some small delay, as the horizontal circulation adjusts to the changes that

the thermodynamical forcing imparts on the vertical motion, and so it might be the case that 6-hourly data do not have a fine enough temporal resolution to capture the delay. Therefore, we conclude from our analysis that if a delay in the dynamical response to latent heating exists, the lag is less than 6 hr.

The typical schematic of a cyclone life cycle focuses on the relative locations of the warm and cold fronts and the central pressure deepening, strengthening the gradient winds. In this context, our results show that precipitation for a single ETC track maximizes prior to the peak in circulation. This result is consistent with the findings of Rudeva and Gulev (2011) and Bengtsson et al. (2009); however, our analysis shows that this lag is because the PWV available to the ETC decreases as the track approaches maximum strength.

As discussed in section 1, one motivation for this analysis is the projected increase in midlatitude moisture due to anthropogenic climate change. This will impact ETCs. Yettella and Kay (2017) show that in one general circulation model, ETC precipitation will increase over the next 100 years, and the change is predominantly due to changes in PWV. The results of our analysis affirm the impact changes in PWV can have on ETC precipitation. Yettella and Kay (2017) also found very little change in the distribution of dynamical strength of ETCs between the end of the 20th and 21st centuries. Our work suggests that the increased precipitation would have a dynamical impact. One possibility is that this impact is offsetting the projected decrease in atmospheric baroclinicity, which is why the cyclone strength remains the same with climate change.

Acknowledgments
The GPM IMERG products were obtained from the NASA Goddard Space Flight Center Precipitation Processing System (PPS) data server; the ERA-Interim products are from the European Center for Medium range Weather Forecast website. The MCMS extratropical cyclone algorithm and documentation are available at http://gcss-dime.giss.nasa.gov/mcms/. C. M. N. and J. F. B. were partially funded by NASA PMM grant NNX16AD82G and NOAA grant NA15OAR4310094.

References

Ahmadi-Givi, F., Graig, G. C., & Plant, R. S. (2004). The dynamics of a midlatitude cyclone with very strong latent-heat release. *Quarterly Journal of the Royal Meteorological Society*, *130*(596), 295–323. https://doi.org/10.1256/qj.02.226

Bauer, M., & Del Genio, A. D. (2006). Composite analysis of winter cyclones in a GCM: Influence on climatological humidity. *Journal of Climate*, *19*(9), 1652–1672. https://doi.org/10.1175/JCLI3690.1

Bauer, M., Tselioudis, G., & Rossow, W. B. (2016). A new climatology for investigating storm influences in and on the extratropics. *Journal of Applied Meteorology and Climatology*, *55*(5), 1287–1303. https://doi.org/10.1175/JAMC-D-15-0245.1

Bengtsson, L., Hodges, K. I., & Keenlyside, N. (2009). Will extratropical storms intensify in a warmer climate? *Journal of Climate*, *22*(9), 2276–2301. https://doi.org/10.1175/2008JCLI2678.1

Booth, J. F., Naud, C. M., & Del Genio, A. D. (2013). Diagnosing warm frontal cloud formation in a GCM: A novel approach using conditional subsetting. *Journal of Climate*, *26*(16), 5827–5845. https://doi.org/10.1175/JCLI-D-12-00637.1

Booth, J. F., Naud, C. M., & Willison, J. (2018). Evaluation of extratropical cyclone precipitation in the North Atlantic Basin: An analysis of ERA-Interim, WRF, and two CMIP5 models. *Journal of Climate*, *31*(6), 2345–2360. https://doi.org/10.1175/JCLI-D-17-0308.1

Catto, J. L., Shaffrey, L. C., & Hodges, K. I. (2010). Can climate models capture the structure of extratropical cyclones? *Journal of Climate*, *23*(7), 1621–1635. https://doi.org/10.1175/2009JCLI3318.1

Chang, E. K. M., & Song, S. W. (2006). The seasonal cycles in the distribution of precipitation around cyclones in the western North Pacific and Atlantic. *Journal of the Atmospheric Sciences*, *63*(3), 815–839. https://doi.org/10.1175/JAS3661.1

Dee, D. P., Uppala, S. M., Simmons, A. J., Berrisford, P., Poli, P., Kobayashi, S., et al. (2011). The ERA-Interim reanalysis: Configuration and performance of the data assimilation systems. *Quarterly Journal of the Royal Meteorological Society*, *137*(656), 553–597. https://doi.org/10.1002/qj.828

Emanuel, K. A., Fantini, M., & Thorpe, A. J. (1987). Baroclinic instability in an environment of small stability to slantwise moist convection. Part I: Two-dimensional models. *Journal of the Atmospheric Sciences*, *44*(12), 1559–1573. https://doi.org/10.1175/1520-0469(1987)044<1559:BIIAEO>2.0.CO;2

Field, P. R., & Wood, R. (2007). Precipitation and cloud structure in midlatitude cyclones. *Journal of Climate*, *20*(2), 233–254. https://doi.org/10.1175/JCLI3998.1

Grecu, M., Olson, W. S., Munchak, S. J., Ringerud, S., Liao, L., Haddad, Z., et al. (2016). The GPM combined algorithm. *Journal of Atmospheric and Oceanic Technology*, *33*, 2225–2245. https://doi.org/10.1175/JTECH-D-16-0019.1

Hawcroft, M., Dacre, H., Forbes, R., Hodges, K., Shaffrey, L., & Stein, T. (2017). Using satellite and reanalysis data to evaluate the representation of latent heating in extratropical cyclones in a climate model. *Climate Dynamics*, *48*(7-8), 2255–2278. https://doi.org/10.1007/s00382-016-3204-6

Hawcroft, M., Shaffrey, L., Hodges, K., & Dacre, H. (2012). How much Northern Hemisphere precipitation is associated with extratropical cyclones? *Geophysical Research Letters*, *39*, L24809. https://doi.org/10.1029/2012GL053866

Held, I. M., & Soden, B. J. (2006). Robust responses of the hydrological cycle to global warming. *Journal of Climate*, *19*(21), 5686–5699. https://doi.org/10.1175/JCLI3990.1

Hoskins, B., & Hodges, K. (2002). New perspectives on the Northern Hemisphere winter storm tracks. *Journal of the Atmospheric Sciences*, *59*(6), 1041–1061. https://doi.org/10.1175/1520-0469(2002)059<1041:NPOTNH>2.0.CO;2

Huffman, G. (2017). GPM IMERG Final Precipitation L3 Half Hourly 0.1 degree x 0.1 degree V05 (GPM-3IMERGHH), Greenbelt, MD, Goddard Earth Sciences Data and Information Services Center (GES DISC), Accessed 2018. https://doi.org/10.5067/GPM/IMERG/3B-HH/05

Huffman, G. J., Bolvin, D. T., Braithwaite, D., Hsu, K., Joyce, R., Kidd, C., et al. (2017). NASA Global Precipitation Measurement (GPM) Integrated Multi-satellitE Retrievals for GPM (IMERG), *Algorithm Theoretical Basis Document* (ATBD) Version 4.6. https://pmm.nasa.gov/sites/default/files/document_files/IMERG_ATBD_V4.6.pdf

Michaelis, A. C., Willison, J., Lackmann, G. M., & Robinson, W. A. (2017). Changes in winter North Atlantic extratropical cyclones in high-resolution regional pseudo–global warming simulations. *Journal of Climate*, *30*(17), 6905–6925. https://doi.org/10.1175/JCLI-D-16-0697.1

Naud, C. M., Booth, J. F., Lebsock, M., & Grecu, M. (2018). Observational constraint for precipitation in extratropical cyclones: Sensitivity to data sources. *Journal of Applied Meteorology and Climatology*, *57*(4), 991–1009. https://doi.org/10.1175/JAMC-D-17-0289.1

Pfahl, S., & Sprenger, M. (2016). On the relationship between extratropical cyclone precipitation and intensity. *Geophysical Research Letters*, *43*, 1752–1758. https://doi.org/10.1002/2016GL068018

Rudeva, I., & Gulev, S. K. (2011). Composite analysis of North Atlantic extratropical cyclones in NCEP-NCAR reanalysis data. *Monthly Weather Review*, *139*(5), 1419–1446. https://doi.org/10.1175/2010MWR3294.1

Skofronick-Jackson, G., Petersen, W. A., Berg, W., Kidd, C., Stocker, E. F., Kirschbaum, D. B., et al. (2017). The Global Precipitation Measurement (GPM) mission for science and society. *Bulletin of the American Meteorological Society*, *98*(8), 1679–1695. https://doi.org/10.1175/BAMS-D-15-00306.1

Stoelinga, M. T. (1996). A potential vorticity-based study on the role of diabatic heating and friction in a numerically simulated baroclinic cyclone. *Monthly Weather Review*, *124*(5), 849–874. https://doi.org/10.1175/1520-0493(1996)124<0849:APVBSO>2.0.CO;2

Ulbrich, U., Leckebusch, G. C., & Pinto, J. G. (2009). Extra-tropical cyclones in the present and future climate: A review. *Theoretical and Applied Climatology*, *96*(1-2), 117–131. https://doi.org/10.1007/s00704-008-0083-8

Wernli, H., & Davies, H. C. (1997). A Lagrangian-based analysis of extratropical cyclones: The method and some applications. *Quarterly Journal of the Royal Meteorological Society*, *123*(538), 467–489. https://doi.org/10.1002/qj.49712353811

Yettella, V., & Kay, J. E. (2017). How will precipitation change in extratropical cyclones as the planet warms? Insights from a large initial condition climate model ensemble. *Climate Dynamics*, *49*(5-6), 1765–1781. https://doi.org/10.1007/s00382-016-3410-2